A&A 420, 361–370 (2004)
DOI: 10.1051/0004-6361:20035899

Astronomy & Astrophysics

Determination of the location and effective angular size of solar flares with a 210 GHz multibeam radiometer

T. Lüthi, A. Lüdi, and A. Magun

Institute of Applied Physics, University of Bern, Sidlerstrasse 5, 3012 Bern, Switzerland
e-mail: [andreas.luedi,andreas.magun]@mw.iap.unibe.ch

Received 18 December 2003 / Accepted 9 March 2004

Abstract. We report on the study and successful application of an improved measurement method for solar flares at millimeter wavelengths. A 210 GHz multibeam receiver for the observation of solar bursts was installed in the KOSMA 3 m telescope on the Gornergrat. It consists of three radiometer channels, with a fourth beam synthesised from the other three. The four intersecting beams allow measurements of source locations with arcsecond resolution and, for the first time, also the determination of the effective source size at short millimeter waves. The typical sensitivity of <1.5 sfu allows also the detection of weak flares at millisecond time resolution. In this paper we present the instrument and the numerical method for the determination of the source flux density, position and effective size, as well as simulations to asses the validity of the method. First observational results were obtained for the GOES X17.2 flare on October 28, 2003. The event reached a peak flux density of 11 000 sfu at 210 GHz and exhibited a slowly varying, time-extended emission from an extended source (effective diameter ≈ 60 arcsec), as well as a short-lived component from a compact source (≲10 arcsec) originating from a different location.

Key words. Sun: activity – Sun: flares – Sun: radio radiation – telescopes – methods: observational

1. Introduction

Solar flares are a consequence of magnetic instabilities in the solar corona. Within seconds to minutes, a large amount of magnetic energy is released into the acceleration of charged particles, shock-waves and heat. A broad spectrum of electromagnetic radiation is emitted, from km-wavelengths to γ-rays. The main radiation mechanisms at short millimeter and submillimeter wavelengths are gyrosynchrotron radiation from ≳0.5 MeV electrons and thermal bremsstrahlung from the hot plasma in the post-flare loops (White & Kundu 1992; Kundu et al. 1990, 1994). Thus, millimeter and submillimeter observations are important diagnostic tools to investigate the acceleration process of electrons at relativistic energies and the hot solar flare plasma. However, the literature on solar flares at millimeter and submillimeter wavelengths is sparse: the increasingly severe and variable absorption of radio waves by the Earth's atmosphere and the strongly rising thermal flux density of the quiet Sun ($\propto \nu^2$) severely limit the sensitivity for the detection of weak solar flares above ~50 GHz (Nakajima et al. 1985; White & Kundu 1992).

One way to improve the signal-to-noise ratio is the use of interferometric techniques. Interferometers are not sensitive to sources larger than about one-third of the fringe spacing, thus the quiet Sun background is cancelled out and the sensitivity to fluctuations of the atmospheric absorption is drastically reduced. Two types of instruments are used. Nulling interferometers for regular patrol observations cancel the quiet Sun component by correlating the signals from two small antennas, reaching a sensitivity of ~10–20 sfu at 80–90 GHz (Nakajima et al. 1985; Lüthi 1999). They are sensitive to flares over the whole solar disc, but do not provide any useful information about the source position or topology. Imaging interferometer arrays like the Berkeley-Illinois-Maryland Array (BIMA) allow spatially highly resolved observations with a very high sensitivity of up to ~0.02 sfu (e.g. Kundu et al. 1990; Silva et al. 1996; Raulin et al. 1999). However, BIMA's time resolution of ~0.4 s is too low for the detection of fast temporal structures attributed to a fragmented energy release (e.g. Kaufmann et al. 1985), and the instrument is insensitive to flux from extended (≳20 arcsec) features. During the extended phase and during gradual events however, thermal source sizes of up to 2.8 arcmin have been observed (Shimabukuro 1970; Lüthi et al. 2003a).

An alternative is the use of a single large antenna with a field of view much smaller than the solar disc, thus reducing the quiet Sun background flux density. Early flare observations with large single-dish antennas were reported by Shimabukuro (1970) and Kaufmann et al. (1985) at 90 GHz. Observations are made either by continuously mapping the solar disc, or by tracking an active region. While mapping of the solar disc permits to locate flare sources at a poor temporal and spatial resolution, the latter technique allows a time resolution in the order of milliseconds combined with a high sensitivity. Due to the narrow field of view however, calibration of such

Send offprint requests to: T. Lüthi,
e-mail: thomas.luethi@mw.iap.unibe.ch

observations requires an accurate knowledge of the source position in respect to the antenna beam. This turned out to be a major difficulty in the analysis of our first solar flare observation at 230 and 345 GHz (Lüthi et al. 2003a) with the telescope of the Köln Observatory for Submillimeter and Millimeter Astronomy (KOSMA). In addition, accurately known source positions are not only needed for flux density calibration but are also essential for comparison with spatially high-resolved Hα, EUV and X-ray observations.

This observational challenge can be addressed by the use of a multibeam antenna with at least 3 beams, which allows the accurate determination of the source position and flux density with high time resolution. The multibeam technique for solar flare observations was originally introduced by Efanov & Moiseev (1967) and is currently applied at 48 GHz in the Itapetinga 13.7 m antenna (e.g. Herrmann et al. 1992; Costa et al. 1995) and at 212 GHz in the Solar Submillimeter Telescope (SST) at El Leoncito (e.g. Kaufmann et al. 1996; Kämpfer et al. 1997). Both instruments use a cluster of feedhorns and radiometers at the focal plane of the telescope in order to generate several antenna beams overlapping approximately at the half-power level. When a point-like source is observed simultaneously with three beams pointing into slightly different directions, the ratios between the measured antenna temperatures and the knowledge of the antenna patterns allow the determination of the angular source position with an accuracy that is up to two orders of magnitude better than the antenna half-power beam width (Herrmann et al. 1992; Costa et al. 1995). Although the impulsive sources observed so far with BIMA were compact ($\lesssim$7 arcsec, e.g. Raulin et al. 1999), the assumption of a point-like source is not necessarily correct, and certainly not for the extended thermal emission (Shimabukuro 1970; Lüthi et al. 2003a). Additionally, due to the high sidelobe level (~-15 dB) originating from the large beam-overlap, the angular range where source positions can be determined unambiguosly is limited approximately to the central area between the three beam maxima (Lüdi 1998; Lüdi & Magun 1999; Giménez de Castro et al. 1999). When a flare is observed with four beams simultaneously however, this ambiguity is considerably reduced and it is also possible to obtain a rough estimate of the source size (Giménez de Castro et al. 1999).

The 48 GHz Itapetinga telescope is a five-beam instrument. However, due to the beam arrangement, most solar flares are observed with only three beams simultaneously. In order to fully exploit the potential of the multibeam technique for solar flare observations, an improved multibeam receiver at 210 GHz for the KOSMA-telescope was developed, the Bernese Multibeam Radiometer for KOSMA (BEMRAK). It employs three beams intersecting at the half-power level, with a fourth beam generated by beam synthesis from the other three. This is not only a very cost-effective way to realise a four-beam instrument, but the fourth beam is also ideally located for solar flare observations (cf. Sect. 2.2). The new receiver is operated simultaneously with the 230/345 GHz receivers of KOSMA. The 210 GHz source position and size are also used for flux density corrections at the former two frequencies (assuming both quantities to be independent of frequency). In this paper we present the new instrument and the numerical method for the determination of the source position and effective size. In order to demonstrate the capabilities of the new instrument observations and results from the giant GOES X17.2 flare on October 28, 2003 are shown.

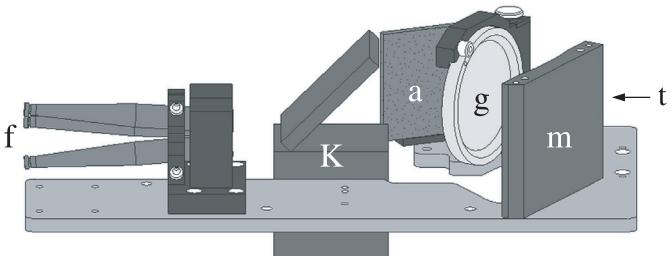

Fig. 1. BEMRAK quasioptics. Radiation from the telescope (t) is transmitted to the 230/345 GHz SIS-receivers (K) as well as reflected by the wire grid (g) and focused by the elliptical mirror (m) into the 210 GHz feedhorns (f). For optimum performance the feedhorns are skewed under ~5 degrees towards the antenna axis. An absorber (a) terminates the unwanted polarisation component of the SIS-receivers.

2. Instrument

The KOSMA 3 m-telescope is located on Gornergrat in the Swiss Alps at 3135 m a.s.l. (Kramer et al. 1998). It is a Cassegrain-type instrument with two Nasmyth ports, one of them equipped with a 230/345 GHz dual-channel SIS-receiver already used for solar observations (Lüthi et al. 2003a). The pointing accuracy of the telescope is typically better than 10 arcsec.

The new multibeam receiver uses three uncooled 210 GHz Schottky mixers. In order to improve the radiometric sensitivity they operate in double-sideband mode with a total radio-frequency (RF) bandwidth of 1 GHz. The integration time constant is 2.3 ms (the same as for the SIS-receivers), which allows the detection of fast temporal structures. All receivers operate in total-power mode and use the quiet Sun and the cold sky as references for absolute flux density calibration (every half-hour). Quiet Sun flux densities are calculated following Croom (1979). A tiltable subreflector periodically deflects the antenna beams in cross-elevation by 6 arcmin from the target to a quiet reference region on the Sun. This "10 s on/0.2 s off" observation cycle allows the compensation of atmospheric attenuation changes with time scales above 10 s. In case of a strong flare automatically switched attenuators reduce the detected signal to avoid saturation, and hence increase the dynamic range of the instrument. Under typical, non-ideal summer conditions (i.e. high humidity levels) a sensitivity of <1.5 sfu was measured (with atmospheric corrections).

2.1. Quasioptical layout

As only one Nasmyth port of the telescope can be used at a given time, BEMRAK has been integrated into the original SIS-receiver setup of KOSMA (Fig. 1). Before entering the different receivers the beam from the telescope (t) is split by

a wire grid (g). The wires are oriented under a projected angle of 45 degrees relative to the support plate, thus the transmitted radiation is linearly polarized under 135 degrees. The 230 and 345 GHz SIS-receivers (K) are sensitive to orthogonal linear polarisations at 0 and 90 degrees, but also detect unwanted radiation reflected by the wire grid. This signal path is terminated by an absorber (a) at room-temperature.

The reflected component is focused by an elliptical mirror (m) into the three 210 GHz feedhorns (f) of the multibeam receiver (polarised under 45 degrees). Low beam distortion and a very compact design is guaranteed by the small reflexion angle of 30 degrees (Goldsmith 1998). The intended antenna pattern directions (beams intersecting at half-power levels) require the beams at the focal plane of the telescope to be nearly parallel with their axes pointing to the corners of an equilateral triangle (Lüdi 1998). Modelling of beam propagation leads to the positions and the skew angles of the feedhorns visible in Fig. 1. As the beam waist radii at the focal plane, the focal length of the elliptical mirror, waist radii and position of the feedhorns etc. are all coupled, an iterative approach was used to determine a suitable set of these parameters. Measurements of the focal plane patterns carried out with a submillimeter vector network-analyser showed a very good agreement with numerical simulations down to the –30 dB level (Lüthi et al. 2003b; Durić et al. 2003).

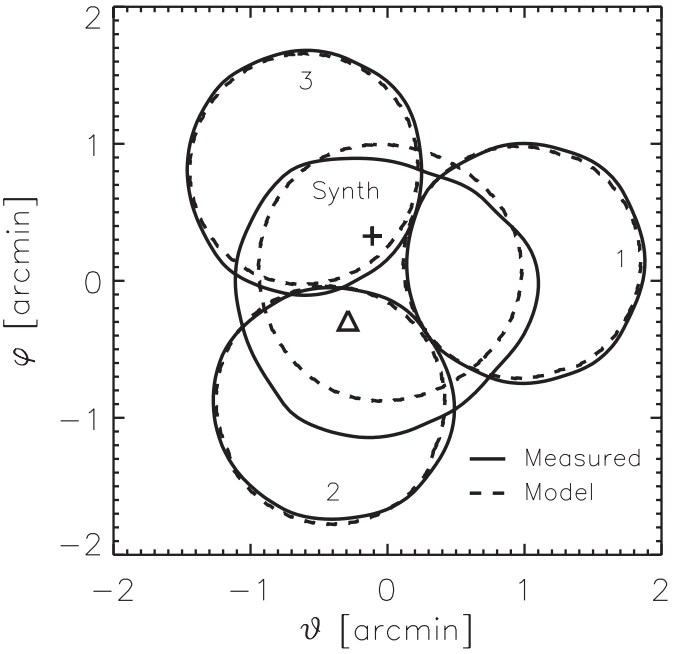

Fig. 2. Simulated and measured antenna patterns (half-power levels). Measurements of beams 1–3 closely agree with the simulations, whereas the synthesised beam shows a slight displacement and broadening due to phase and amplitude differences of the IF-signals prior to combination (that are not taken into account by the simulation). Also indicated are the centre positions for the 230 and 345 GHz beams determined from solar maps (cross and triangle, respectively).

2.2. Beam synthesis

A conventional four (or more) beam instrument, for which all beams lie side by side (e.g. Herrmann et al. 1992), will observe a flare source only in a maximum of three beams with large gain. Thus the field of view usable for the analysis of a burst source with four beams is very limited (Giménez de Castro et al. 1999). A synthesised fourth beam on the other hand is centred on the beam cluster (Fig. 2), so that all four beams exhibit a large gain towards a source located near the central region of the beams. As the most cost-relevant parts of a radiometer are the mixers and feedhorns, this is also a very cost-effective way to realise a four beam receiver.

Beam synthesis requires coherency, thus a single local oscillator (LO) is used to drive all three mixers with a LO-power distribution network (Fig. 3). The down-converted intermediate-fequency (IF) signals are split and then additively combined with an IF-combining network to form the synthesised beam. After quadratic detection four output-voltages U_{i} are obtained that are proportional to the respective flux densities observed with the four beams.

In order to produce a well defined, circular synthesised beam in the centre of the other three beams, the IF-signals must have similar amplitudes and only small phase differences prior to combination. Numerical simulations indicate that amplitude differences below 2 dB and a total phase difference below 60 degrees are sufficient for a well defined beam. For amplitude matching each radiometer channel is equipped with a variable attenuator that was set during the initial tests. Phase matching must be done in the RF and the IF-part of the instrument separately, as both sidebands are used. The sign of the down-converted RF phase difference is sideband-dependent, hence the correction in the IF-part alone could only satisfy one sideband. Therefore LO-power distribution and IF-combining networks with identical path-lengths for all channels are employed. For the phase adjustments we used a test transmitter to produce a quasi plane-wave at the feedhorn apertures and compared the down-converted signals with a vector network-analyser. The observed phase differences were minimised by slightly moving individual feedhorns back and forth, which has only negligible influence on the antenna patterns. Phase differences in the IF-part were directly measured with a vector network-analyser and minimised by adapting the cable length. After adjustments the amplitudes of the IF-signals agree within 1 dB and the phases within 60 degrees (over both sidebands).

2.3. Antenna pattern measurements

Antenna pattern measurements with a signal-to-noise ratio $\gtrsim$35 dB were carried out over a distance of 6.5 km, which is approximately half the far-field distance. No notable differences of the main beam and first sidelobes to the true far-field patterns are expected (Lüdi 1998). The test transmitter was mounted on another mountain top and tuned to several different frequencies within both sidebands. For the three "real" beam patterns there are no differences, and the synthesised beam pattern shows only minor differences between sidebands. As the flux density of a solar flare over the small relative bandwidth of the instrument (2%) is basically constant, it is evident to use beam patterns averaged over both sidebands for data analysis.

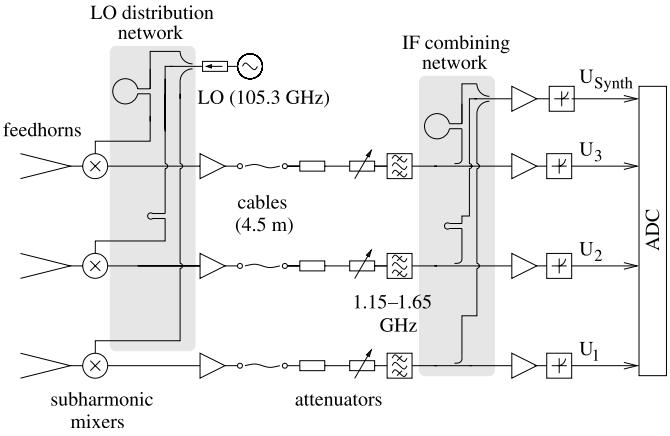

Fig. 3. Block diagram of BEMRAK. A single local-oscillator and a LO-power distribution network is used to drive all three mixers. The IF-signals are split and then additively combined with an IF-combining network to form the synthesised beam. Automatically switched attenuators increase the dynamic range in order to avoid saturation during strong flares.

Figure 2 shows the averaged antenna patterns as well as the results of numerical modelling. The half-power beam widths are 1.7 arcmin for beams 1–3 and 2.1 arcmin for the synthesised beam. Beams 1–3 intersect each other at the half-power level and closely agree with numerical simulations within the first nulls. The first sidelobes however exhibit an asymmetry with a maximum at –12 dB. The synthesised beam shows a slight displacement and broadening in respect to the simulated one. This is due to the phase and amplitude differences of the IF-signals mentioned above, that have not been taken into account for the simulation.

The relative positions of the 230 and 345 GHz beams were determined from maps of the solar disc which showed them well centred between beams 1–3. Scans over the solar limb also allowed an estimate of the half-power beam widths in respect to broadband noise. The resulting values at 210 GHz agree well with the ones determined using the test transmitter, and at 230 and 345 GHz half-power beam widths of 2.0 and 1.5 arcmin were found. As the limb scans revealed no significant asymmetry, symmetrical Gaussians are used for the analysis of 230 and 345 GHz data.

3. Data analysis

The quiet Sun brightness-temperature of ~6300 K at 210 GHz (Linsky 1973) is far above the temperature range covered by the cold and ambient-temperature loads (77 and ~280 K) normally used for the calibration of the KOSMA-receivers. Therefore we do not attempt to determine antenna temperatures, but directly calculate the flux densities using the cold sky and a quiet region on the solar disc as calibration references. The flux density S_{obs_i} observed by the antenna beam i of a multibeam instrument is then

$$S_{\mathrm{obs}_i} = \frac{U_i - U_{\mathrm{ref}_i}}{U_{\mathrm{ref}_i} - U_{\mathrm{sky}_i}} S_{\odot_i}, \qquad (1)$$

where U_i, U_{ref_i} and U_{sky_i} are the signals measured at the flare source, the reference region and the cold sky, respectively. The observed quiet Sun flux density $S_{\odot_i}$ is determined from the measured antenna power pattern P_{n_i} and the quiet Sun brightness temperature. Equation (1) takes into account all losses of the antenna and the absorption by the Earth's atmosphere and the Goretex membrane protecting the telescope from visible and infrared radiation.

The flux density S_{obs_i} of an arbitrary source, which is observed by the antenna beam i, is given by the convolution between the source excess brightness-temperature distribution T_{B} and the normalised antenna pattern P_{n_i} (e.g. Kraus 1966):

$$S_{\mathrm{obs}_i}(\vartheta,\varphi) \propto \iint T_{\mathrm{B}}(\vartheta',\varphi') P_{\mathrm{n}_i}(\vartheta'-\vartheta,\varphi'-\varphi)\,\mathrm{d}\Omega. \qquad (2)$$

Early studies on multibeam antennas (e.g. Herrmann et al. 1992; Costa et al. 1995) assumed point sources and symmetrical Gaussian antenna patterns. Giménez de Castro et al. (1999) introduced an extended source brightness-temperature distribution of symmetrical Gaussian shape. This allows not only the determination of the source location, but also an estimate of the source size: when a flare is observed in four beams simultaneously, Eq. (2) forms a system of four equations with four unknowns (position, source diameter and burst intensity) that can be solved straightforward. However, due to the beamshape uncertainty of the antenna, the source size could not be determined reliably so that the method was used only to distinguish between point-like and extended sources. Additionally, due to the lack of a centre beam only very few events were observed in more than three beams.

BEMRAK, on the contrary, observes basically all events with four beams simultaneously, and the antenna patterns are accurately known. As the approximation with symmetrical Gaussian beams can lead to considerable errors (Lüdi & Magun 1999), a new numerical algorithm was developed in order to fully exploit the data.

3.1. Description of algorithm

The method developed for the computation of the source position and size from the observed flux densities is fully numerical and uses measured beam patterns. It compares calculated flux density ratios between different channels with the measured ones and searches for the position and source size for which the best agreement is obtained. Once the position and effective size of the flare has been determined, the flux densities observed by the individual beams are corrected in order to obtain the total flare flux density (i.e. the burst intensity). Basically, the method is similar to the one introduced by Herrmann et al. (1992), but includes the source size as an additional parameter.

The antenna patterns have been measured with a grid spacing of down to 3 arcsec and are interpolated to a spacing of 1 arcsec. On a grid of 264 × 264 arcsec^2 the flux density $F_{i,k}(\vartheta_0,\varphi_0)$ observed by beam i from an assumed excess source brightness-temperature distribution T_{B_k} is calculated at each grid position (ϑ_0,φ_0), following Eq. (2). In principle, any source geometry can be used, but for the sake of simplicity and due to the lack of a priori information about the source topology, a symmetrical Gaussian source with a half-power width HPW_{flare_k} is assumed. In case of a non-Gaussian source

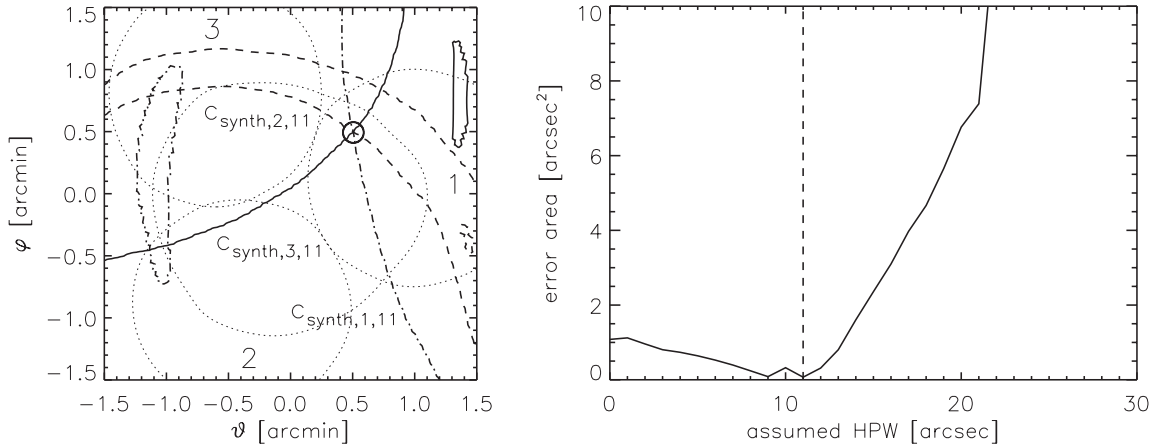

Fig. 4. Reconstruction of the source position and size for a simulated Gaussian source centred on $(\vartheta, \varphi) = (0.5 \text{ arcmin}, 0.5 \text{ arcmin})$ and a source diameter of 10 arcsec. The curves $c_{\text{synth},j,11}$ correspond to the positions for which simulated and modelled flux density ratios are equal (left side, for an assumed source diameter of 11 arcsec). Their intersection point corresponds to the inferred source position (circle). The figure on the right side shows the area of the error-triangle for different assumed source sizes which reaches minimum for an assumed source size of 11 arcsec.

our method thus yields the centre of emission and an effective source size (cf. Sect. 3.2).

For each pair of beams (i, j) the expected flux density ratios $F_{i,k}/F_{j,k}$ for a given source position (ϑ_0, φ_0) and source diameter HPW_{flare_k} are calculated. The locations, where this ratio is equal to the observed flux density ratio $S_{\text{obs}_i}/S_{\text{obs}_j}$, form a curve $c_{i,j,k}$ where the source must be located:

$$\frac{F_{i,k}(\vartheta_0(c_{i,j,k}), \varphi_0(c_{i,j,k}))}{F_{j,k}(\vartheta_0(c_{i,j,k}), \varphi_0(c_{i,j,k}))} = \frac{S_{\text{obs}_i}}{S_{\text{obs}_j}}, \quad i \neq j. \tag{3}$$

With four beams one obtains 6 curves, of which only three are independent. We use the three combinations that incorporate the synthesised beam (Fig. 4, left side). This avoids combinations of two beams observing the source both with a low gain which make the derived source position and effective size more vulnerable to noise.

In most cases, the source location curves do not intersect each other in a single point, but form a triangle of intersection points. As the actual source position $(\vartheta_{0_k}, \varphi_{0_k})$ we use the barycentre of the triangle. So far, the algorithm corresponds to the method used by Lüdi & Magun (2002) to determine the angle of arrival of a transmitter signal during atmospheric measurements. Additionally, we also take into account the area A_k of the triangle, as it depends on the assumed source size HPW_{flare_k} and becomes minimal for the actual source size (Fig. 4, right side). Thus, the procedure of finding $(\vartheta_{0_k}, \varphi_{0_k})$ and A_k is repeated for different source sizes. For a first overview, typically source sizes from 0 to 90 arcsec are assumed and varied in steps of 6 arcsec. Smaller steps strongly increase computation time, and for sources much larger than the antenna beams no reliable results can be expected any more.

It should be noted that the source position $(\vartheta_{0_k}, \varphi_{0_k})$ found for a given source diameter is not unambiguous. In many cases there results more than one possible source location. However, numerical simulations have shown that this ambiguity is considerably reduced by the use of four beams instead of only three (Fig. 5). In addition, basically all except one of these regions of

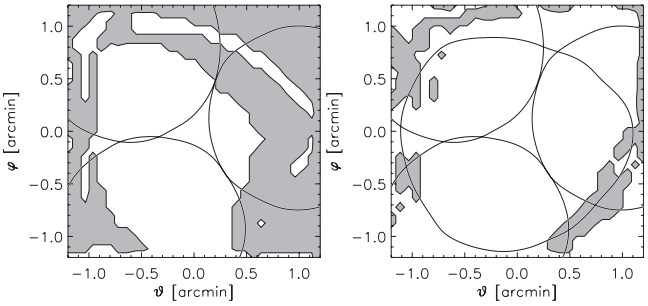

Fig. 5. Ambiguity of the inferred source position for a point source. Gray areas denote source positions for which more than one source location is inferred. The ambiguity area is considerably reduced by the use of four beams (*right*) instead of only three (*left*).

ambiguity are located far away from the centre of the beam cluster. If the source position is approximately known by other means, the range of acceptable source locations can be limited and the inferred location can be trusted. This a priori information of the source location can be obtained e.g. by a map of the solar disc after the event (assuming that the source location remains constant within a few arcmin), or simultaneously with the tracking observations from the analysis of the detected flux densities during the movement of the beams to the reference region: if at least one beam is moved across the source, its location can be roughly estimated.

The source position and effective size determined by the algorithm described above is then also used for the flux density calibration of the 230 and 345 GHz data. The latter beams are assumed to be symmetrical Gaussians whose half-power widths and centres in respect to the 210 GHz beam-pattern are determined from limb scans and solar maps (Fig. 2). Assuming that the location and effective size of the radio-source are independent of frequency, the observed flux densities are corrected in order to obtain the total flare flux density (Lüthi et al. 2003a). Due to the small difference in frequency in respect to the multibeam-instrument, these assumptions are most

probably correct for the 230 GHz channel. However, they might not always be valid for 345 GHz: at least during the thermal phase of a flare significant differences in source size between 230 and 345 GHz have been observed (Lüthi et al. 2003a). However, as long as the observed effective source size is much smaller than the half-power beam width of the telescope (as it is expected for the impulsive phase of a flare) this is uncritical, as then the influence of the actual source size on the inferred flux density is negligible.

3.2. Simulations

Our algorithm allows the determination of the source location (i.e. the centre of emission for an extended source), flux density and effective source size. In order to asses the validity of this method numerous simulations have been carried out. We have convolved the measured beams with an assumed source brightness distribution and calculated the resulting observed flux densities S_{obs_i} for different source positions in a box of 3×3 arcmin^2. For symmetrical Gaussian sources with half-power widths between 0 and 90 arcsec, the simulated and inferred positions agree within 1 arcsec, and the error of the inferred source size is below ∼10%. These small uncertainties are due to rounding errors of the numerical algorithm.

For a second set of simulations we have added random noise to each channel. The noise level $\Delta U/U$ was set to 0.4%, as actually measured during daytime in summer (high humidity), and thus represents worst-case conditions. As impulsive sources are thought to be compact (e.g. Raulin et al. 1999), a Gaussian source with a half-power width of 10 arcsec was assumed. The total source flux density was set to 0.5, 1 and 2 times the observed quiet Sun value. For each flux density level and grid point, the simulation was run 250 times (corresponding to approximately 0.5 s of data), and the mean values and scatter (standard deviation) for the source position and diameter were computed. The error maps for the strongest source are shown in Fig. 6. Within the limits of the half-power contour of the synthesised beam, the systematic errors of the inferred mean source position and diameter are less than 1 arcsec and 2 arcsec, respectively. The scatter of the inferred source position is below 1 arcsec within the area of the synthesised beam, whereas the source diameter exhibits a scatter of ∼3 arcsec. Both, systematic error and scatter increase with decreasing flare strength. Hence for weak events the observed flux densities should be integrated prior to analysis, especially in order to obtain an accurate estimate of the effective source size, which is less robust towards noise than the source location. We also tested our algorithm with other source diameters (5 and 30 arcsec) and found similar results. The absolute systematic error and scatter of the inferred source diameter are approximately constant for all sources, thus the relative accuracy of the source size estimate improves for larger sources.

Our method assumes symmetrical Gaussian sources which is an idealisation. In a simple flare model mm/submm radiation is emitted by relativistic electrons in a magnetic loop. Depending on the actual field-strength distribution, the high-frequency radiation is either emitted from the whole loop or concentrated near its footpoints. Hence we probably either face an elongated source or two separated ones. For the first flare observed with KOSMA (Lüthi et al. 2003a) hard X-ray images showed two footpoints ∼25 arcsec apart. We thus simulated the response of our method towards asymmetric sources, either composed of two separated sources, or of "cigar" shape (Fig. 7). For the twin source, symmetrical Gaussians with a half-power width of 10 arcsec and separated by 20 and 30 arcsec were assumed. The inferred effective source size corresponds within ∼10% to the separation of the single sources, considerably overestimating the source area. For a fragmented source the inferred effective diameter thus represents an upper limit for the total source area. On the other hand, the centre of emission and flux densities are correctly determined within 7 arcsec and 10%, respectively. The elongated source is composed of several symmetrical Gaussians of 10 arcsec width, overlapping each other at the 1/e-level (Giménez de Castro et al. 1999). For a source length of 16, 20 and 35 arcsec the inferred effective source size corresponds within ∼20% to a circular source with the same half-power area as the simulated one, and the location of the source centre and flux density are correct within 4 arcsec and 5%, respectively. During the thermal phase of a solar flare however, much more extended sources have been observed (Shimabukuro 1970; Lüthi et al. 2003a). We thus also modelled elongated sources of 30×60 arcsec^2 and 60×120 arcsec^2. Especially for the latter the results are slightly worse. The effective source size is

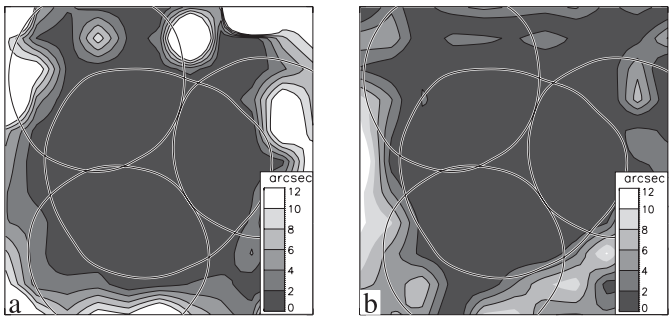

Fig. 6. Error maps of the source location **a)** and size **b)**. The gray-scaled maps show the systematic error of the inferred mean emission-centre position and of the mean inferred source diameter. The noise level was set to 0.4% (corresponding to an integration time constant of 2.3 ms), with a simulated source diameter and flux density of 10 arcsec and two times the observed quiet Sun value, respectively.

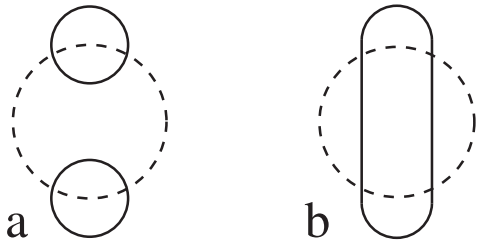

Fig. 7. Simulated (solid) and inferred (dotted) sources (half-power levels). For two separated sources **a)**, the inferred source size corresponds to the separation angle, thus overestimating the source area. The inferred size for the elongated source **b)** corresponds to a symmetrical source of the same half-power area.

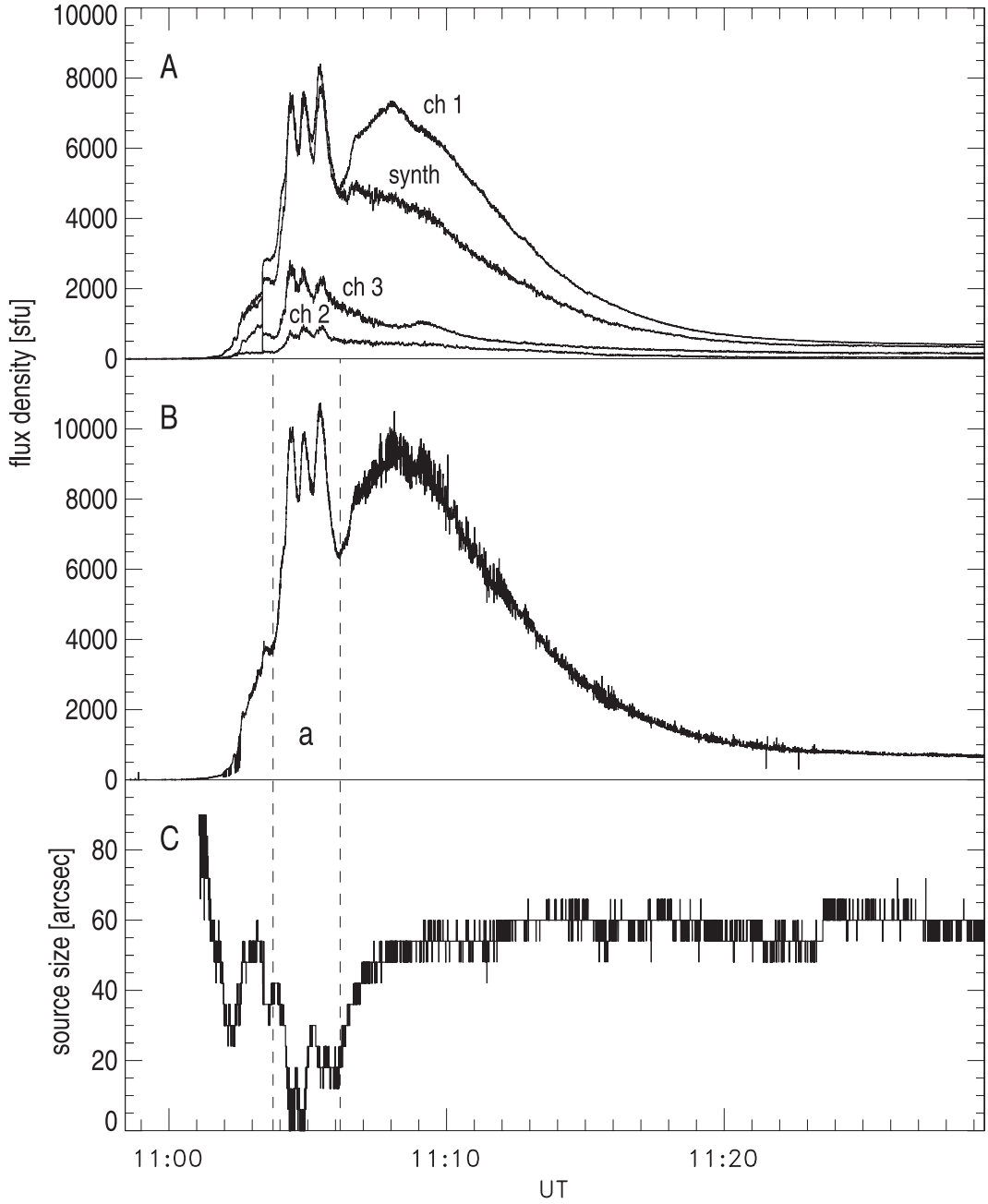

Fig. 8. Flux density time profiles and effective source diameter for the X17.2 flare on October 28, 2003. Calibrated flux densities of the four BEMRAK channels (panel **A**, ch 1–3, synth), inferred 210 GHz total flux density (panel **B**) and source size (panel **C**). Phase a is characterised by enhanced emission from a compact source. The raw data has been integrated over 0.1 s prior to analysis.

correct within ~20%, the position error increases to 20 arcsec and the inferred flux density differs from the simulated one by up to 30%.

Although the algorithm assumes a symmetrical Gaussian source, it can also be applied to strongly asymmetric sources. However, our simulations clearly show that the method works better for compact sources.

4. Observations

During the period of exceptionally high solar activity in October 2003 four events were observed, two of them right from the beginning. Figure 8 shows the flux density time profiles and effective source diameters for the giant GOES X17.2 burst on October 28. The tracking-observations were interrupted between 11:29 and 12:00 UT in order to obtain solar maps. For the current analysis the time profiles have been integrated over 0.1 s. The calibrated flux density time profiles observed by the four beams (panel A) exhibit large differences in amplitude and shape. This illustrates the advantage of multi-beam observations, as without the knowledge of the relative source position, the reconstruction of the total flux density (panel B) would have been very difficult.

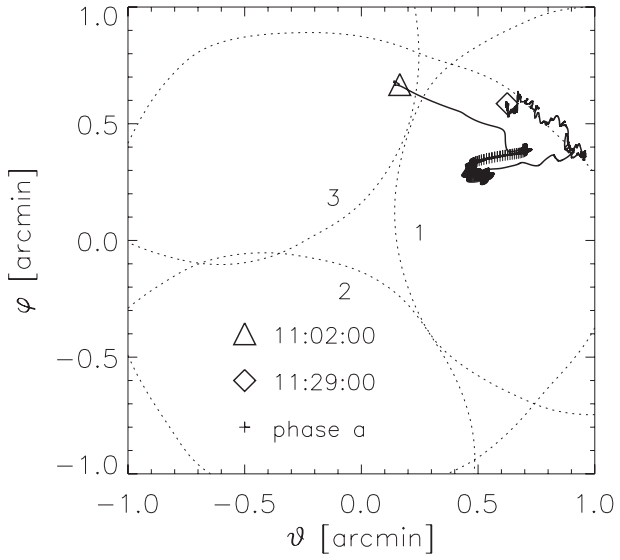

Fig. 9. Mean source location during the flare on October 28, 2003, from 11:02 to 11:29, integrated over 10 s. The crosses indicate the inferred positions during phase a, which exhibit a significant difference to the mean position of the extended source.

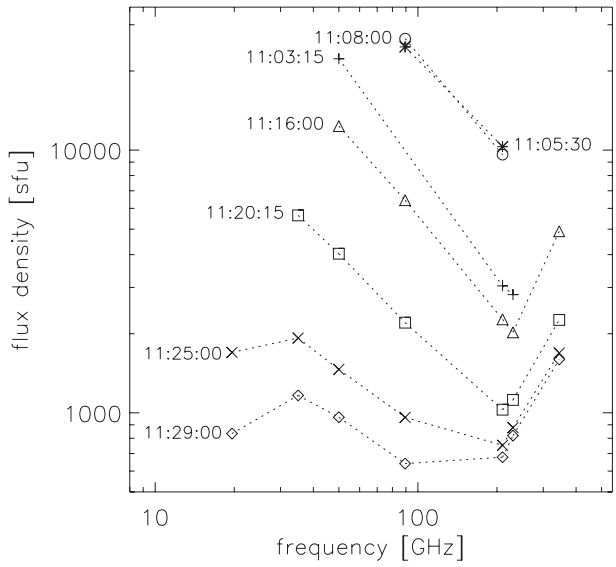

Fig. 10. Temporal evolution of the radio spectrum between 19.6 and 345 GHz (10 s averages). Missing data points mean that the respective instrument was saturated or calibrating. The flux density errors are 15% at 19.6–89.4 GHz, and <20%, +60/–20% and +100/–30% at 210, 230 and 345 GHz, respectively (worst case).

Emission at 210 GHz was first detected as a slow rise in intensity at ∼11:00. After a dramatic increase at ∼11:02:30, an enormous peak flux density of 11 000 sfu was reached at 11:05:25. The total flux density time profile exhibits two main features: a slowly varying, time-extended component lasting from 11:02:30 to ∼11:20, and a short-lived component exhibiting three distinctive peaks between 11:03:45 and 11:06:10 (phase a). The slowly decreasing emission after 11:20 was detected until at least 14:30. From the solar maps a flux density of ∼600 sfu is obtained at 11:40, which is in reasonable agreement with the 650 sfu at the end of the tracking observations (11:29).

Most of the time the inferred effective source size is approximately 60 arcsec (Fig. 8, panel C). During phase a however, the source appears to be compact or even point-like (≲10 arcsec). The source position (Fig. 9) shows distinctive changes. For clarification it has been integrated over 10 s, thus all fast movements (due to either atmospheric seeing or true source movement) are smoothed out. In general, the source is located between beams 1 and 3 which is consistent with the observed flux density changes during subreflector scans. At the beginning of the flare, the emission centre moves steadily towards the centre of beam 1. During phase a however, the centre of emission is shifted ∼15 arcsec away from the position immediately before the onset of the first peak. After the third peak the source location slowly returns to the position before phase a again. The same slow return to pre-phase a levels is also observed for the effective source size (Fig. 8). This behaviour of the source location and size can be explained by a slowly varying and extended source on which a short-lived compact one is superimposed. As soon as the additional emission dominates the total brightness distribution, a compact source is observed. If the centres of emission are not coincident, also a shift of the inferred source location is expected. When the flux density of the compact source decreases again, both the inferred source position and effective size return to their previous values. TRACE-data (195 Å) shows two ribbons of ∼90 arcsec length and an arcade of loops covering an area of $\sim 120 \times 60$ arcsec^2. The extended source might represent emission from the whole arcade (or from the ribbons that are made up from the footpoints of the individual loops), whereas the compact source corresponds to one or more exceptionally strong flaring loops. Unfortunately the telescope pointing suffered from a constant but unknown offset (≲60 arcsec) so that a direct comparison of source positions is not possible.

There are no significant differences between the spectra emitted by the extended and the compact sources. Figure 10 shows that the instantaneous frequency spectra (10 s averages) during the third peak (11:05:30) and at the maximum of the extended emission (11:08:00) are almost identical. However, the spectral coverage of this event is somewhat limited: our 89.4 GHz nulling interferometer did an automatic calibration until 11:05:30, and the Bumishus patrol instruments (8.4–50 GHz, Lüthi et al. 2003a) as well as the 230/345 GHz KOSMA-channels were saturated part of the time due to the enormous flux density of the event. Only BEMRAK recorded a complete time profile, due to the automatically switched attenuators which provided the necessary dynamic range. Thus there is no spectral information available between 11:04:00 and 11:05:30. Aside from this gap in the spectral coverage, the spectrum has its maximum below 50 GHz, with a radio spectral index between –1.4 and –0.9 throughout the impulsive phase of the event. These spectra can be interpreted as the optically thin part of a gyrosynchrotron spectrum. After 11:20, the spectrum gets increasingly flatter, which is indicative for optically thin thermal free-free emission. Remarkably, the 345 GHz flux density measured after 11:16 is approximately twice the 210 GHz value. During the impulsive phase, the 230 GHz flux

density fits into the spectral slope seen at the lower frequencies. After 11:20 however, it is larger than the flux density at 210 GHz and closely follows the spectral slope between 210 and 345 GHz. So far, no explanation for this particular feature has been found, but rising spectra in the millimeter and submillimeter range have also been reported for the GOES X28 burst on November 4, 2003 (Kaufmann et al. 2004).

Error estimation

During this event, atmospheric conditions were slightly better than the ones used for the simulations. Immediately before the flare start a noise level $\Delta U/U$ of 0.3% was measured. As the flux density was $\gtrsim 3\ S_\odot$ throughout the time interval shown in Fig. 8 ($\sim 40\ S_\odot$ during phase a), the noise-induced errors are considerably smaller than the ones found from the simulations. Unfortunately, a large, asymmetric source of 120×60 arcsec^2, as seen in the TRACE-images, could cause large errors of the inferred source position and effective size. However, the radio source is not necessarily identical to the EUV source. Additionally, the simulations using a large, asymmetric source clearly result in a much larger inferred effective source size than 60 arcsec. Therefore we can safely assume that the impulsive mm-source is considerably smaller than 120×60 arcsec^2 and that the errors of the relative source position and effective size are well below 10 arcsec and 20%, respectively. Taking also into account the uncertainty of the observed flux density from the reference region, the error of the inferred flux density is estimated to be 20%. During phase a the source is compact, thus the errors of the inferred flux density and relative source position are considerably lower ($\lesssim$10% and 3 arcsec, respectively).

The absolute error of the source position unfortunately is much larger. Due to a pointing problem, the position of the beam pattern on the solar disc is only known within ~1 arcmin, an offset that is constant throughout the event. This again highlights the importance of a multibeam instrument for such observations, as the knowledge of the relative source position still allows accurate calibration of the data.

The flux density errors at 230 and 345 GHz are caused mainly by uncertainties of the half-power beam widths determined from limb-scans and the 210 GHz source position. The assumption of a frequency-independent source location appears to be correct, as the solar maps at ~11:40 indicate that the 210, 230 and 345 GHz sources are co-located within 6 arcsec. Based on the above uncertainties, the relative flux density errors at 230 and 345 GHz for a symmetrical 60 arcsec-source are estimated to be +25/–10% and +50/–10%, respectively. For the largest elongated source the errors lie within +60/–20% and +100/–30%. The remarkably strong flux density at 345 GHz can not be explained by these errors, especially as they tend to increase it even more.

5. Conclusions

We have developed an improved multibeam receiver for the KOSMA telescope for solar flare observations in the millimeter and submillimeter range. The new instrument is a cluster of three 210 GHz receivers, with a fourth beam hardware-synthesised from the other three. This is not only a very cost-effective way to realise a four-beam instrument, but the fourth beam is also ideally located for solar flare observations. As it lies in the centre of the beam cluster basically all flare sources are observed with four beams simultaneously. This is highly advantageous for source recovery. Four-beam observations considerably reduce the ambiguity of the inferred source position and also allow an estimate of the effective source size. Assuming a frequency-independent source location and size, also the calibration of the 230/345 GHz (single beam) observations is possible.

The new method developed for the determination of the total flux density, source location and effective diameter is fully numerical and takes into account the accurately measured antenna patterns. Numerous simulations have shown that it works well in a box of 3×3 arcmin^2 centred on the beam cluster. Taking into account the worst-case noise, the usable area is limited approximately to the half-power area of the synthesised beam (2×2 arcmin^2). Errors increase with decreasing flare strength, but are considerably reduced by integration of the observed flux densities prior to analysis. Although the algorithm assumes symmetrical Gaussian sources, also the main features (position, effective size and flux density) of strongly asymmetric sources are determined reliably. Minimum errors are obtained for compact sources.

One of the first events observed with the new instrument is the giant GOES X17.2 burst on October 28, 2003. The flux density time profile shows two main features: a slowly varying, time-extended component from an extended source (~60 arcsec), and a short-lived component from a compact source with an effective diameter of less than ~10 arcsec. The emission centres of the compact and extended sources differ by ~15 arcsec. TRACE images show an arcade of loops covering an area of $\sim 120 \times 60$ arcsec^2, thus the extended source might represent emission from the whole arcade, whereas the compact source corresponds to one or more exceptionally strong flaring loops. The spectra of the extended and compact source are almost identical, however, spectral coverage is somewhat limited as most other instruments were partially saturated. During the two main components, the radio spectral index varies from –1.4 to –0.9. After ~11:20 we observe a slowly decreasing, long-lived emission with an increasingly flat spectrum, as characteristic for optically thin thermal free-free emission. Remarkably, the spectrum is rising strongly above 210 GHz.

This event clearly demonstrates the value of the new instrument and observational method. In spite of an unknown tracking offset, accurate flux density calibration was possible due the known source position relative to the telescope axis. For the first time the effective source size of an impulsive flare has been determined at such high radio frequencies. The quantitative analysis including other data such as optical, EUV and X-ray observations (RHESSI) is subject of a future study.

Acknowledgements. We wish to express our thanks to Dr. A. Murk, V. Vasić and D. Weber (IAP, University of Bern) for their assistance in the phase and antenna pattern measurements. The authors also appreciate the assistance of the KOSMA team, especially Dr. M. Miller

(University of Cologne), in telescope operation. This research is funded by the Swiss National Science Foundation under the grant 200020-100167. The KOSMA 3 m radio telescope at Gornergrat-Süd Observatory is operated by the University of Cologne and supported by special funding from the Land Nordrhein-Westfahlen. The Observatory is administered by the Internationale Stiftung Hochalpine Forschungsstationen Jungfraujoch und Gornergrat, Bern. TRACE-data was provided by the Solar Data Analysis Center at NASA Goddard Space Flight Center.

References

Costa, J. E. R., Correia, E., Kaufmann, P., Magun, A., & Herrmann, R. 1995, Sol. Phys., 159, 157

Croom, D. L. 1979, Jan. 1, Solar Flare Millimetre Data, Appleton Laboratory, Ditton Park, Slough, England

Durić, A., Lüthi, T., & Vasić, V. 2003, IAP Research Report 2003-18, Institute of Applied Physics, University of Bern, Switzerland

Efanov, V. A., & Moiseev, I. G. 1967, The Observational Method of Solar Radio Emission Bursts by Sharp-Directional Aerials, Russian Academy of Science

Giménez de Castro, C. G., Raulin, J.-P., Makhmutov, V. S., Kaufmann, P., & Costa, J. E. R. 1999, A&AS, 140, 373

Goldsmith, P. F. 1998, Quasioptical Systems (IEEE Press)

Herrmann, R., Magun, A., Costa, J. E. R., Correia, E., & Kaufmann, P. 1992, Sol. Phys., 142, 157

Kämpfer, N., Magun, A., Feist, D., et al. 1997, in 6th International Symp. on Recent Advances in Microwave Technology Proc., Beijing, China

Kaufmann, P., Correia, E., Costa, J. E. R., Zodi Vaz, A. M., & Dennis, B. R. 1985, Nature, 313, 380

Kaufmann, P., Costa, J. E. R., Correia, E., et al. 1996, in Coronal Physics from Radio and Space Observations (Springer Lecture Notes in Physics), 483

Kaufmann, P., Raulin, J.-P., Gimenez de Castro, C. G., et al. 2004, ApJ, 603

Kramer, C., Degiacomi, C. G., Graf, U. U., et al. 1998, in Proc. SPIEE, 3357, 711

Kraus, J. D. 1966, Radio Astronomy (McGraw-Hill)

Kundu, M. R., White, S. M., Gopalswamy, N., Bieging, J. H., & Hurford, G. J. 1990, ApJ, 358, L69

Kundu, M. R., White, S. M., Gopalswamy, N., & Lim, J. 1994, ApJS, 90, 599

Linsky, J. L. 1973, Sol. Phys., 28, 409

Lüdi, A. 1998, Master's Thesis, Institute of Applied Physics, University of Bern, Switzerland, http://www.iapmw.unibe.ch/publications/pdffiles/138.pdf (in German)

Lüdi, A., & Magun, A. 1999, IAP Research Report 1999-03, Institute of Applied Physics, University of Bern, Switzerland, http://www.iapmw.unibe.ch/publications/pdffiles/189.pdf

Lüdi, A., & Magun, A. 2002, Radio Science, 37, 12.1, doi: 10.1029/2001RS002493

Lüthi, T. 1999, Master's Thesis, Institute of Applied Physics, University of Bern, Switzerland, http://www.iapmw.unibe.ch/publications/pdffiles/189.pdf

Lüthi, T., Magun, A., & Miller, M. 2003a, A&A, 415, 1123 [doi:10.1051/0004-6361:20034624]

Lüthi, T., Murk, A., Magun, A., Lüdi, A., & Vasić, V. 2003b, in The 28th International Conference on Infrared and Millimeter Waves, ed. N. Hiromoto, 219

Nakajima, H., Sekiguchi, H., Sawa, M., Kai, K., & Kawashima, S. 1985, PASJ, 37, 163

Raulin, J.-P., White, S. M., Kundu, M. R., Silva, A. V. R., & Shibasaki, K. 1999, ApJ, 522, 547

Shimabukuro, F. I. 1970, Sol. Phys., 15, 424

Silva, A. V. R., White, S. M., Lin, R. P., et al. 1996, ApJ, 458, L49

White, S. M., & Kundu, M. R. 1992, Sol. Phys., 141, 347